A robust source-independent full-waveform inversion

Xin Fu and Kris Innanen

ABSTRACT

Full-waveform inversion (FWI) can reconstruct high-resolution underground velocity and lithology structures even under complex geological backgrounds, and has been widely developed. But a reliable real-data inversion generally needs accurate source wavelet information, which is still one of the major challenges in FWI. In this paper, a robust source-independent FWI method is developed, which is demonstrated via synthetic tests of different starting models, different true models, different levels of random noises, and different types of source wavelets. It does not require any prior source wavelet information. It does not require an accurate starting model, even a 1D starting model is feasible to output an accurate wavelet estimate. It is stable for random noises. A good estimate of the source wavelet can be obtained from a poorly converged model based on the new proposed wavelet estimation equation. All in all, the performance of the new source-independent FWI in the synthetic data tests is close to that of the known-source-wavelet FWI.

INTRODUCTION

Full-waveform inversion (FWI), simultaneously using the kinematic and dynamic information of pre-stack seismic data, can reconstruct high-resolution underground velocity and lithology structures even under complex geological backgrounds, and has been widely developed (Lailly et al., 1983; Tarantola, 1984; Mora, 1987; Bunks et al., 1995; Pratt et al., 1998; Pratt, 1999; Shin et al., 2001; Sirgue and Pratt, 2004; Virieux and Operto, 2009; Fichtner, 2010; Wu et al., 2014; Warner and Guasch, 2016). But a reliable real-data inversion generally needs accurate source wavelet information, which is still one of the major challenges in FWI. The effective source wavelet in a field seismic survey is a cooperation of the source, the subsurface medium, and the receivers. Whereas, the coupling between the source and the subsurface medium, and the coupling between the receivers and the subsurface medium are normally ill-informed (Lee and Kim, 2003).

To avoid the requirement of inputting an accurate source wavelet in the conventional known-source-wavelet (KSW) FWI method, several source-independent methods have been proposed, including the deconvolution-based method, the convolution-based method, and the iterative estimation of source signature (IES) method (Zhang et al., 2016). The deconvolution-based method is proposed by Lee and Kim (2003) using a single reference trace to normalize the wavelet information in the wavefield, and Zhou and Greenhalgh (2003) conducting the normalization with the average amplitude of the entire common shot gather. The convolution-based method is proposed in frequency domain by Cheong et al. (2004) and Choi et al. (2005) and in time domain by Choi and Alkhalifah (2011), in which the observed wavefield is convolved with the reference trace selected from the synthetic seismogram, and the synthetic wavefield is convolved with the reference trace selected from the observed seismogram; the source wavelet difference between the observed wavefield and the synthetic wavefield is eliminated, since both have a double source wavelet, i.e., the convolution between source wavelets of the observed wavefield and the synthetic seismogram. But in both deconvolution- and convolution-based methods, the extra calculation for the gradient is required, which is more complicated than that in the conventional KSW FWI (Virieux and Operto, 2009). A more straightforward way is the IES method (Song et al., 1995; Pratt, 1999) which is more commonly used in practice. Unfortunately, all methods mentioned above are sensitive to noise (Xu et al., 2006; Choi and Alkhalifah, 2011; Choi and Min, 2012). Zhang et al. (2016) suppress the noises induced by the convolution process by using a time window on the reference traces for the convolution-based method, which can also simplify the gradient calculation in this method; however, carefully selecting the reference traces and the time window in this method makes it too complicated.

In this paper, we will propose a new source-independent method, which is based on the frame of the IES method but employs a new source wavelet estimation formula. It reserves the merit of easy operation of the conventional IES method but overcomes its demerit of requiring an accurate initial starting model. And the new method is more stable on noise. In the synthetic data test using the modified acoustic Marmousi model, the performance of the new source-independent method is similar to that of the KSW method.

THEORY

A standard FWI (Lailly et al., 1983; Tarantola, 1984) in time domain is normally minimizing the time-domain L2 norm misfit function:

$$E(\mathbf{m}) = \frac{1}{2}||\mathbf{d}_{obs} - \mathbf{F}(\mathbf{m}, \mathbf{w})||_2^2, \tag{1}$$

where $\mathbf{d}_{obs}$ is the observed data or recorded wavefields, $\mathbf{F}(\cdot)$ is a forward modeling operator based on the wave equation to generate the synthetic data that depends on the updating model $\mathbf{m}$ (e.g., P-wave velocity), and the source wavelet $\mathbf{w}$.

By a linearized optimization (e,g, steepest descent method, conjugate gradient method, etc.), the model is updated iteratively as:

$$\mathbf{m}^k = \mathbf{m}^{k-1} + \delta\mathbf{m}^k, \tag{2}$$

where k is the iteration number, and

$$\delta\mathbf{m}^k = -\mu^k \mathbf{g}(\mathbf{m}^{k-1}, \mathbf{w}^{k-1}), \tag{3}$$

in which $\mathbf{g}(\mathbf{m}^{k-1}, \mathbf{w}^{k-1})$ is the opposite updating direction of model in iteration k, which depends on the updated model $\mathbf{m}^{k-1}$ and the source wavelet $\mathbf{w}^{k-1}$ in iteration $k-1$, and μ^k is the corresponding step-length. For different optimizations, it has different calculations, for instance, in the steepest descent method, $\mathbf{g}$ represents the gradient of the misfit function (equation 1) with respect to $\mathbf{m}$ and $\mathbf{w}$, which is the zero-lag cross-correlation between forward wavefileds and backward wavefields of data residuals. For the first iteration, a starting model $\mathbf{m}^0$ and a starting source wavelet $\mathbf{w}^0$ have to be prepared. The starting model can be obtained by velocity analysis or tomography.

In the KSW FWI, $\mathbf{w}$ is treated as a known variable, set before the inversion processing, and kept constant during the inversion. For a numerical FWI example, $\mathbf{m}^0$ is mostly assumed to be accurate. Realistically, it needs to be estimated from the field data, which is difficult to be accurate. In contrast, in the IES FWI, $\mathbf{w}$ is considered as an unknown variable updated during the inversion by (Song et al., 1995; Pratt, 1999):

$$\hat{w}^k(\omega) = \frac{\sum_{i=1}^{n} \hat{d}_{obs}(\omega, i) conj(\hat{G}^k_{syn}(\omega, i))}{\sum_{i=1}^{n} \hat{G}^k_{syn}(\omega, i) conj(\hat{G}^k_{syn}(\omega, i))}, \tag{4}$$

where $\hat{w}$ is $\mathbf{w}$ in frequency domain, $\hat{d}$ is $\mathbf{d}_{obs}$ in frequency domain, ω is the angular frequency, i is the trace (or receiver) number, n is the total number of traces, $conj(\cdot)$ is the conjugate operator, and $\hat{G}^k_{syn}$ is the frequency-domain synthetic green's function calculated by $\mathbf{F}$ using Dirac function as the input soure wavelet and $\mathbf{m}^k$ as the input model. The equation above is derived by assuming $\mathbf{m}^k$ is the true model. However, noises in $\hat{w}$ are not only raised from the inaccurate model, but also from the data noise and the imperfect forward modeling (e.g., Green's function is calculated imprecisely).

To supress the noises in the source wavelet estimated by equation 4, we propose a new equation to update the wavelet, which is:

$$\hat{w}^k(\omega) = \frac{1}{n} \sum_{i=1}^{n} \frac{\hat{d}_{obs}(\omega, i) conj(\hat{G}^k_{syn}(\omega, i))}{\hat{G}^k_{syn}(\omega, i) conj(\hat{G}^k_{syn}(\omega, i))}. \tag{5}$$

Different from equation 4 in which only one source wavelet is calculated for entire traces, equation 5 calculates one source wavelet for each trace first, then takes the average of all wavelets. It assumes that the noises, in the wavelets calculated for different traces, from all kinds of sources are zero-mean, so they can be suppressed after taking the average. A similar equation can be seen in Fu and Innanen (2022), which is employed to eliminate the source wavelet non-repeatability in time-lapse seismic data.

Note, the elements in equations 4 and 5 are in the frequency domain, for the case of performing a time-domain FWI, all related data should be converted to the frequency domain by Fourier transfer, and then calculate the wavelet frequency by frequency, and finally use the inverse Fourier transfer to obtain the time-domain source wavelet. A unit source will be used to calculate the Green's functions. And the estimated wavelet should be properly scaled because of the imperfect forward modeling. In this study, we will typically use a time-domain constant-density acoustic finite-difference method as the forward modeling operator, the steepest descent method as the optimization, and the gradient is preconditioned with the diagonal approximation of the Hessian matrix (Shin et al., 2001). In the following text, for convenience, we will call equation 4 "the old equation", and equation 5 "the new equation". Accordingly, the IES FWI method using equation 4 is referred to as "the old method", and the IES FWI method using equation 5 is referred to as "the new method".

NUMERICAL EXAMPLES

Tests using different starting models

In this subsection, a true modified acoustic Marmousi model (Figure 1a) and four different starting models including starting model 1 (Figure 1b), starting model 2 (Figure 1c),

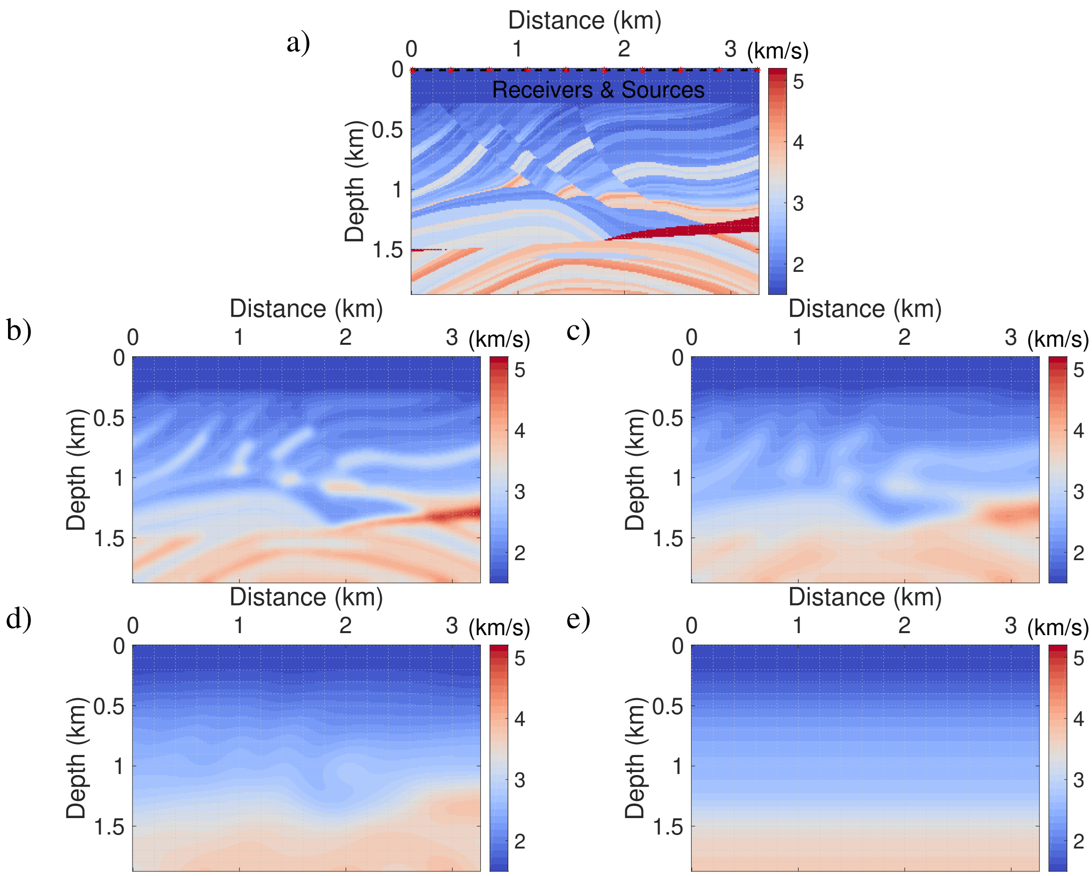

FIG. 1. (a) True model (P-wave velocity) and acquisition geometries, (b) starting model 1, (c) starting model 2, (d) starting model 3, (e) starting model 4. Models 1 to 4 become smoother and smoother, and starting model 4 is 1D. The dash lines and asterisks in (a) are the locations of receivers and sources, respectively.

a)
b)
c)
d)

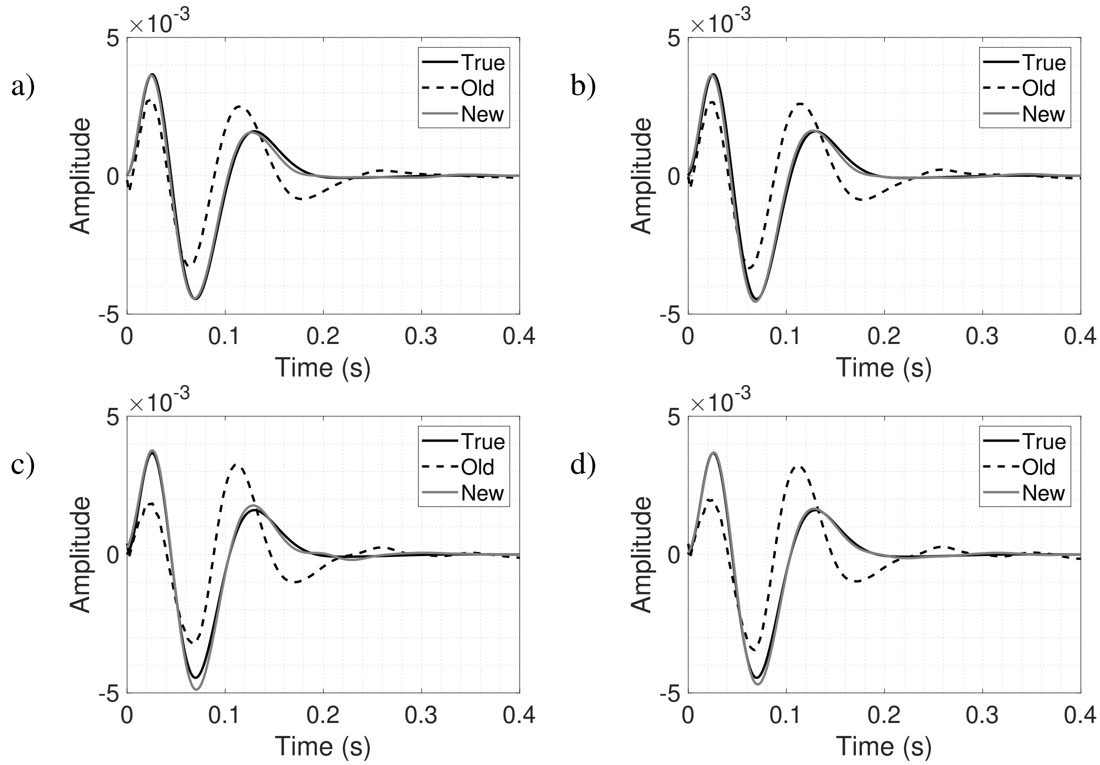

FIG. 2. The final estimated source wavelets of the old method (the IES FWI method using equation 4) and the new method (the IES FWI method using equation 5) using starting models 1 (a), 2 (b), 3 (c), and 4 (d), respectively. In each panel, the black line is the true source wavelet, the dashed line is estimated from the old method, and the gray line is estimated from the new method.

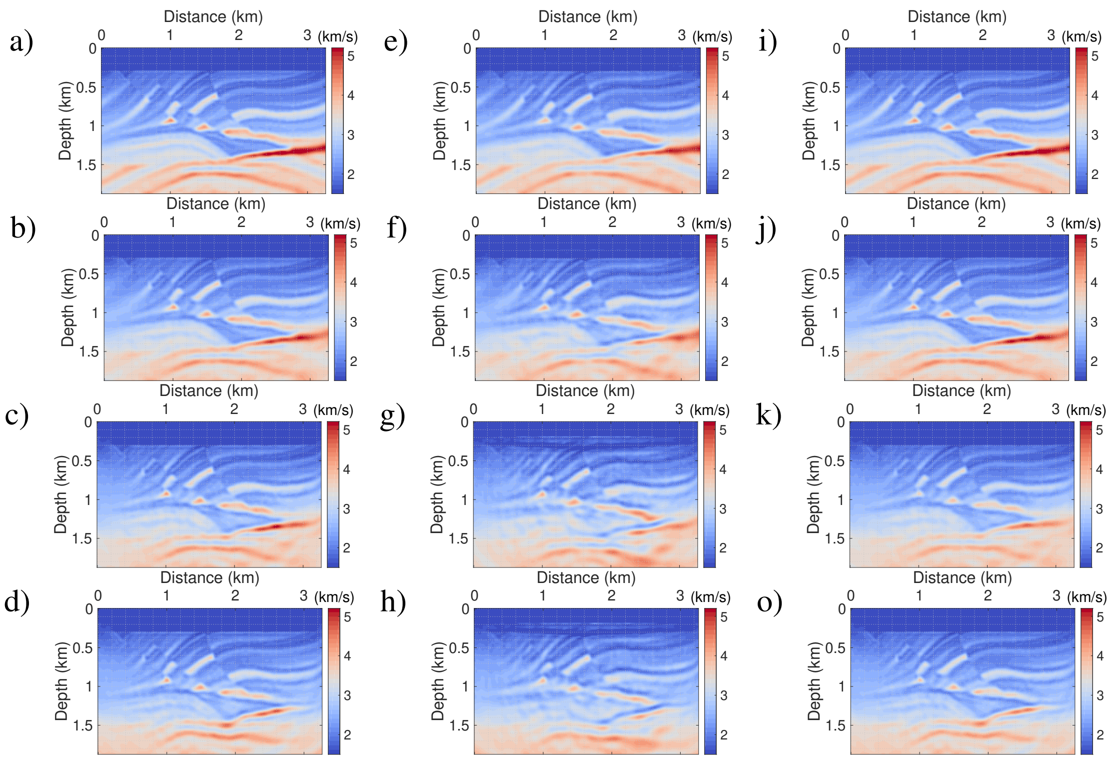

FIG. 3. The first column is the final inverted results of the KSW method (using the true wavelet) using starting models 1 (a), 2 (b), 3 (c), and 4 (d), respectively. The second column is the final inverted results of the old method using starting models 1 (e), 2 (f), 3 (g), and 4 (h), respectively. The third column is the final inverted results of the new method using starting models 1 (i), 2 (j), 3 (k), and 4 (o), respectively.

starting model 3 (Figure 1d), and starting model 4 (Figure 1e) are employed to test the new method, have it be compared with the old method and the KSW method. The starting models become less accurate as the number increases, starting models 1-3 are produced by directly smoothing the true model, and the starting model 4 is 1D. And the acquisition geometry is displayed in Figure 1a. The true model is of a size of 188-by-327, with spacing of 10m. And on its top, ten sources are evenly spread, and 327 receivers are separately set on each surface grid of the model. The true source wavelet used to generate the corresponding synthetic observed data is an 8Hz minimum phase wavelet (the black line in Figure 2).

The final estimated source wavelets of the old and new methods using starting models 1, 2, 3, and 4, respectively, are plotted in Figure 2a-d. And the corresponding final inverted models of the old method and the new method are plotted in Figure 3e-o, and results of the KSW method using different starting models are plotted in Figure 3a-d as references. In Figure 4a-d, traces extracted at distances 1.5km and 2.5km from the results shown in Figure 3a-o are plotted. And curves of the data misfit versus the iteration number for the three different methods using starting models 1, 2, 3, and 4, respectively, are plotted in Figure 5a-d.

From Figures 2-5, we observe the source wavelets estimated from the new method are apparently better than that from the old method and are very close to the true source wavelet. With the accuracy decreasing of the starting model, the inverted results of the old method get worse and become farther from the ones of the KSW method. In contrast, the results of the new method are less impacted by the accuracy of the starting models and are very close to the results of the KSW method. And the data misfits of the new method also have much better convergence than that of the old method, they can converge to a level as low as that of the KSW method.

In Figure 6, the evolution of estimated wavelets of the new method using starting model 3 is displayed. We observe the source wavelet estimate is already very good at iteration 5, and the inverted result of iteration 5 is plotted in Figure 7, which is poorly converged. It means that using a smooth model is good enough to calculate a relatively accurate source wavelet via the new equation.

Tests on noisy data sets

In this subsection, the same true model (1a) as the last subsection and starting model 3 (1d) are used to implement the tests. Different from the noise-free data applied in the last subsection, three noisy synthetic observed data sets with SNRs (signal-to-noise ratios) of 5dB, 2dB, and 1dB, respectively, will be employed here. And the central common shot gathers of them are plotted in Figure 8a-c, respectively.

The final estimated source wavelets of the old and new methods using data sets with SNRs of 5dB, 2dB, and 1dB, respectively, are plotted in Figure 9a-c. And the corresponding final inverted models of the old method and the new method are plotted in Figure 10d-i, and results of the KSW method using data with different noise levels are plotted in Figure 10a-c as references. In Figure 11a-c, traces extracted at distances 1.5km and 2.5km from the results shown in Figure 10a-i are plotted. And curves of the data misfit versus the

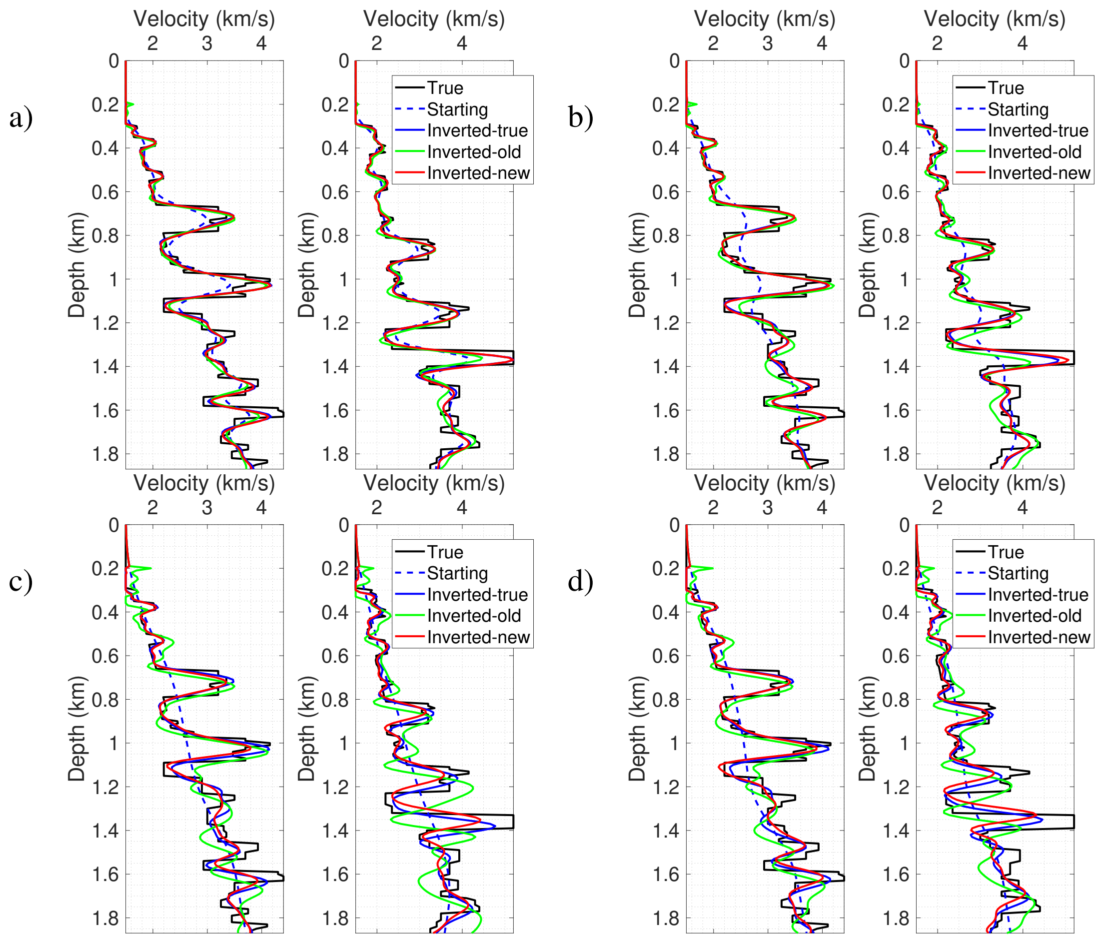

FIG. 4. Traces extracted at distances 1.5km and 2.5km from the results shown in Figure 3. (a), (b), (c), and (d) are inverted traces of different methods using starting models 1, 2, 3, and 4, respectively. In each panel, the solid black line is the true model, the dashed blue line is the starting model, the solid blue line is the result of the KSW method, the solid green line is the result of the old method, and the solid red line is the result of the new method.

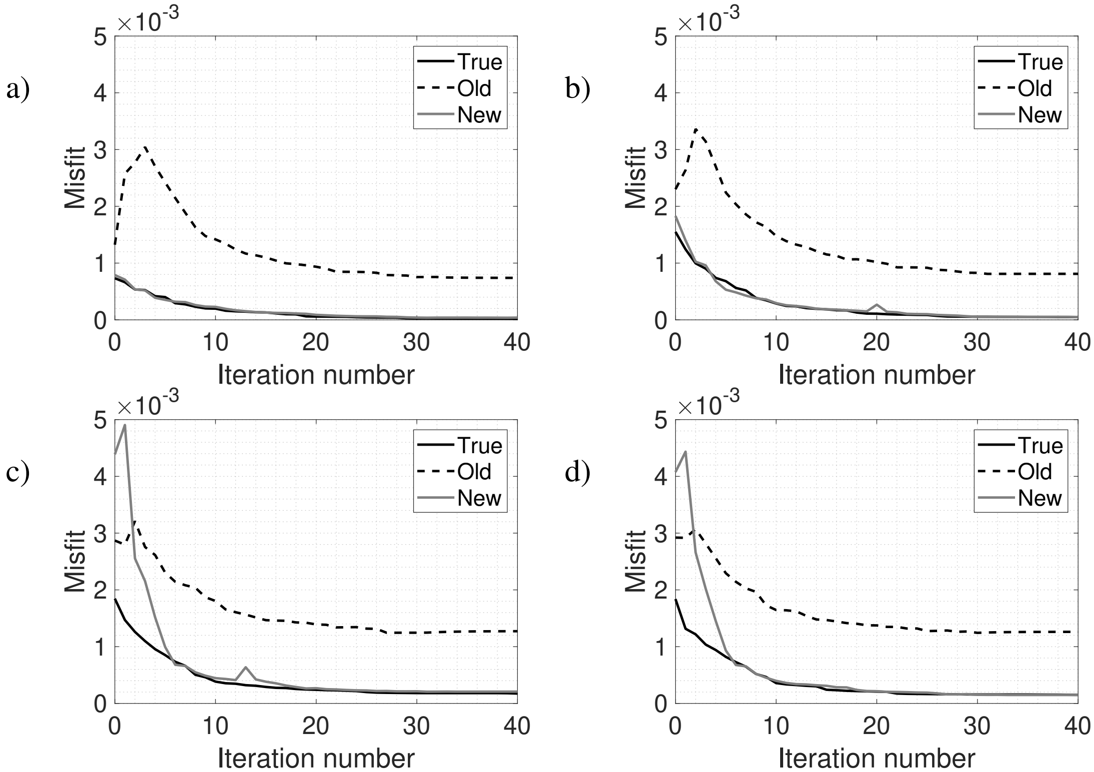

FIG. 5. Curves of the data misfit versus the iteration number for different methods using starting models 1 (a), 2 (b), 3 (c), and 4 (d), respectively. In each panel, the black line is the data misfit curve for the KSW method, the dashed line is the data misfit curve of the old method, and the gray line is the data misfit curve of the new method.

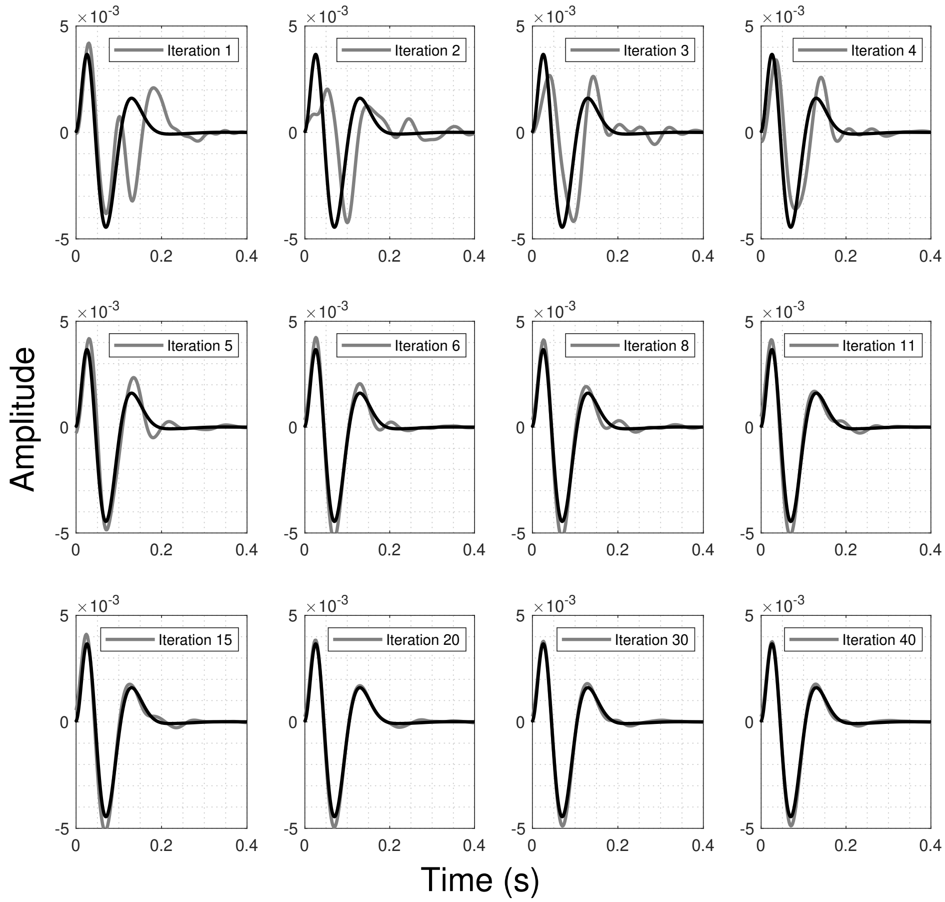

FIG. 6. The evolution of estimated wavelets of the new method. The black line and the dashed line in each panel are the true wavelet and the estimated wavelet at a certain iteration, respectively.

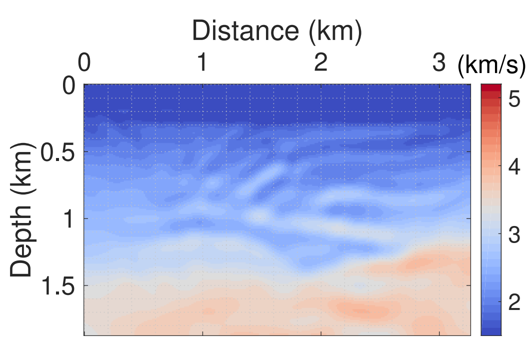

FIG. 7. The result of the new method at iteration 5, and the corresponding estimated source wavelet is plotted in Figure 6.

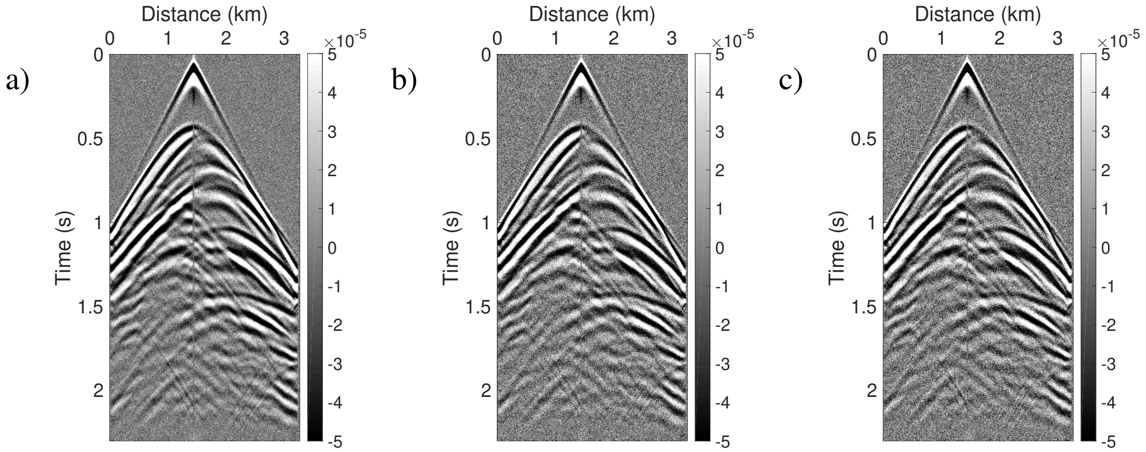

FIG. 8. Noisy shot gathers. (a) SNR=5dB, (b) SNR=2dB, and (c) SNR=1dB.

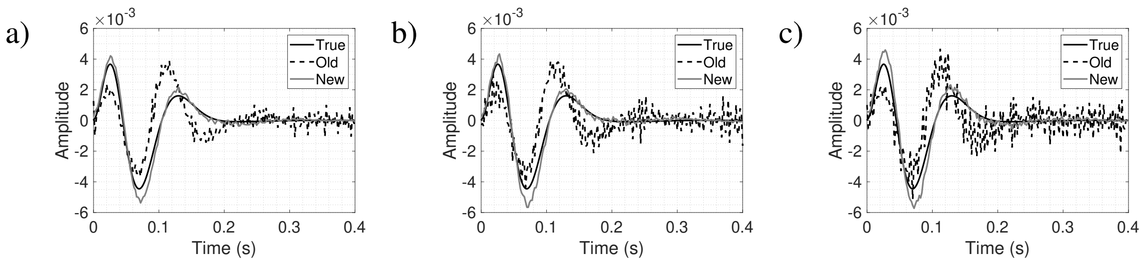

FIG. 9. The final estimated source wavelets of the old method and the new method using noisy data of SNR = 5dB (a), SNR = 2dB (b), and SNR = 1dB (c), respectively. In each panel, the black line is the true source wavelet, the dashed line is estimated from the old method, and the gray line is estimated from the new method.

iteration number for the three different methods using data sets with three different noise levels are, respectively, plotted in Figure 12a-c. From Figures 9-12, we observe the new method has obviously better performance than the old method, is still close to the KSW method, and can stably output source wavelets that match the true wavelet well, when the estimated source wavelets of the old method come with serious perturbation because of the noises.

Tests using different source wavelets

In this subsection, an acoustic overthrust model (Figure 13a) and a smooth starting model (Figure 13b) are employed to test the new method, the old method, and the KSW method. Different from the model in Figure 1a the overthrust model has no water layer, hence, the impact of shot footprints on the inversion will be taken into account in the following tests. And the acquisition geometry is displayed in Figure 13a. The true model is of a size of 152-by-310, with spacing of 15m. And on its top, 13 sources are evenly spread, and 310 receivers are separately set on each surface grid of the model. The true source wavelets used to generate the synthetic observed data sets are, respectively, an 8Hz minimum phase wavelet (wavelet 1, the black line in Figure 14a), an 8Hz Ricker wavelet (wavelet 2, the black line in Figure 14b), an 1Hz-3Hz-15-20Hz Ormsby wavelet (wavelet 3, the black line in Figure 14c).

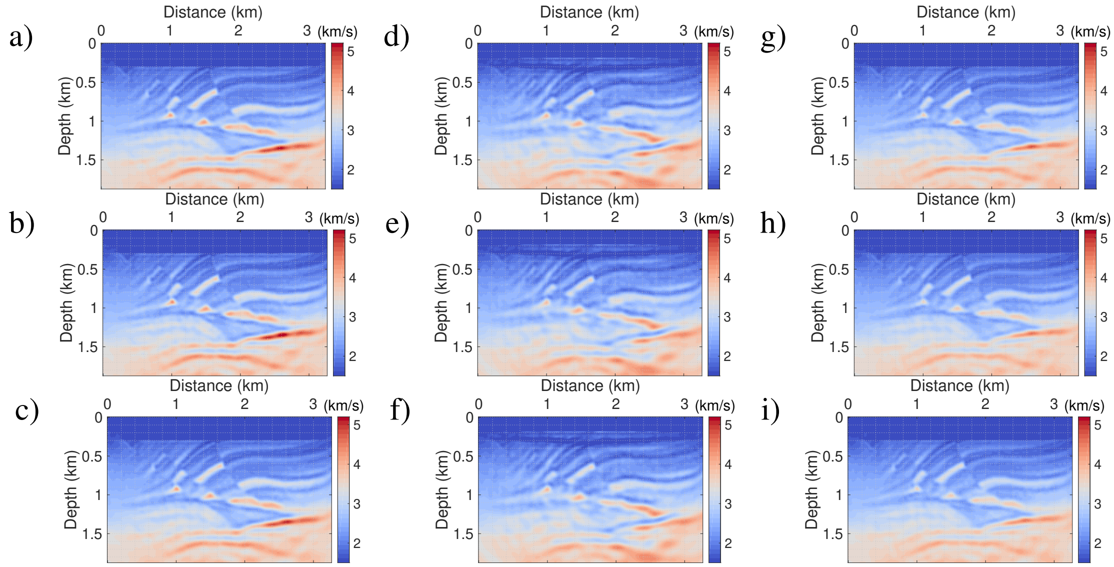

FIG. 10. The first column is the final inverted results of the KSW method using starting models 3 and noisy data of SNR = 5dB (a), SNR = 2dB (b), and SNR = 1dB (c), respectively. The second column is the final inverted results of the old method using starting models 3 and noisy data of SNR = 5dB (d), SNR = 2dB (e), and SNR = 1dB (f), respectively. The third column is the final inverted results of the new method using starting models 3 and noisy data of SNR = 5dB (g), SNR = 2dB (h), and SNR = 1dB (i), respectively.

The final estimated source wavelets of the old and new methods using observed data sets generated with wavelets 1, 2, and 3, respectively, are plotted in Figure 14a-c. And the corresponding final inverted models of the old method and the new method are plotted in Figure 15d-i, and results of the KSW method using data with different wavelets are plotted in Figure 15a-c as references. In Figure 16a-c, traces extracted at distances 1.5km and 2.5km from the results shown in Figure 15a-i are plotted. And curves of the data misfit versus the iteration number for the three different methods using data with different wavelets, respectively, are plotted in Figure 17a-d.

From Figures 14-17, we observe the three source wavelets estimated from the new method are still better than that from the old method and are close to the three true source wavelets. The inverted results and the data misfits of the new method are still superior to that of the old method, and they are still very similar to that of the KSW method. Moreover, the results have demonstrated good adaption of the new method on different wavelets and different models.

Implementation of elastic FWI

The new method is also expended to elastic FWI in this subsection. In Figure 18a-f, true and starting models are displayed. And the inverted results of the old and new methods are plotted in Figure 19a-f. From the results, we can obviously observe that the new method is superior to the old method, and its results can match the true models well. And for more details about the frequency-domain elastic algorithm please refer to Fu et al. (2020).

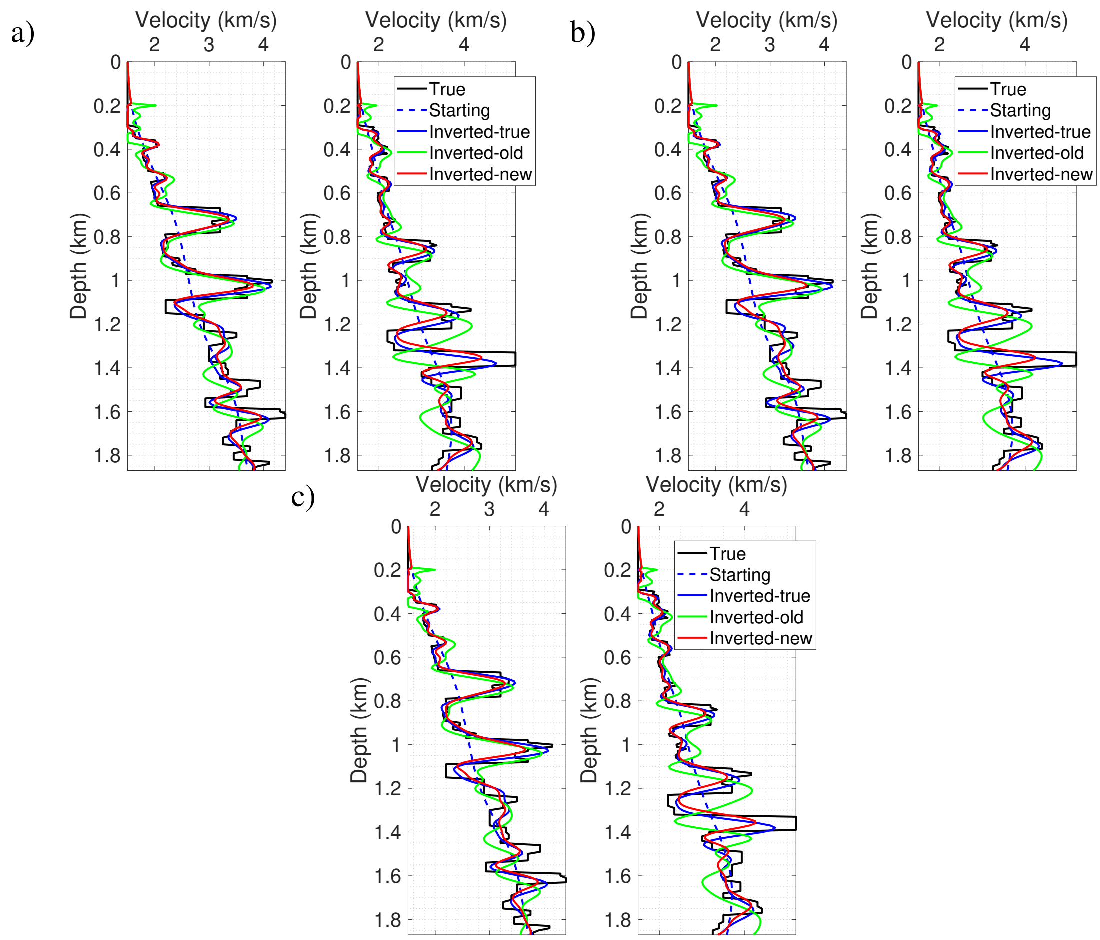

FIG. 11. Traces extracted at distances 1.5km and 2.5km from the results shown in Figure 10. (a), (b), and (c) are inverted traces of different methods using noisy data of SNR = 5dB, SNR = 2dB, and SNR = 1dB, respectively. In each panel, the solid black line is the true model, the dashed blue line is the starting model, the solid blue line is the result of the KSW method, the solid green line is the result of the old method, and the solid red line is the result of the new method.

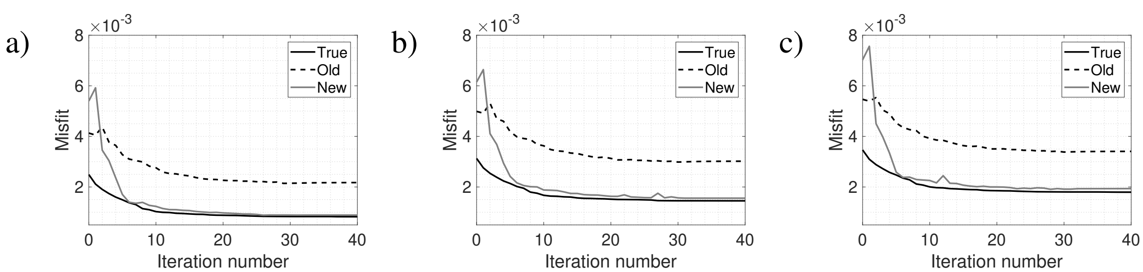

FIG. 12. Curves of the data misfit versus the iteration number for different methods using starting model 3 and noisy data of SNR = 5dB (a), SNR = 2dB (b), and SNR = 1dB (c), respectively. In each panel, the black line is the data misfit curve for the KSW method, the dashed line is the data misfit curve of the old method, and the gray line is the data misfit curve of the new method.

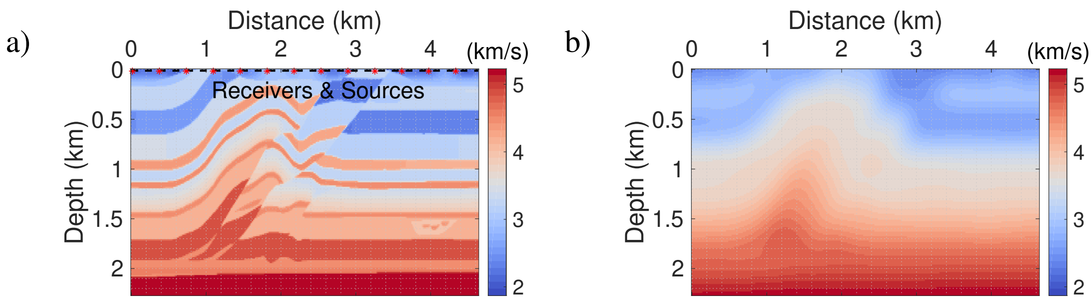

FIG. 13. (a) True overthrust model (P-wave velocity) and acquisition geometries, (b) starting model. The dash lines and asterisks in (a) are the locations of receivers and sources, respectively.

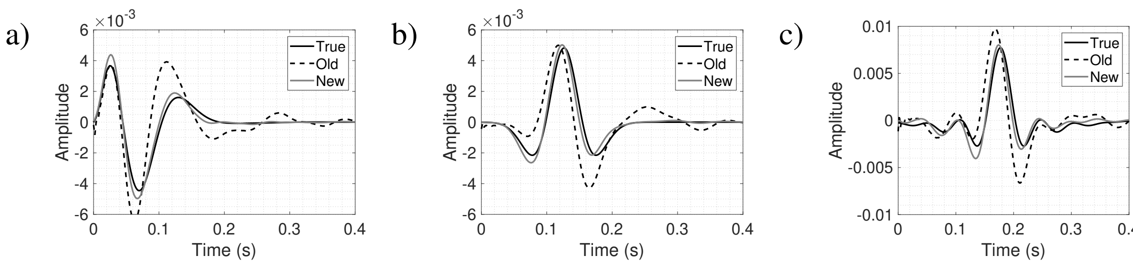

FIG. 14. The final estimated source wavelets of the old and new methods using observed data of the true overthrust model. The data are obtained by using wavelet 1 (a), wavelet 2 (b), and wavelet 3 (c), respectively. In each panel, the black line is the true source wavelet, the dashed line is estimated from the old method, and the gray line is estimated from the new method.

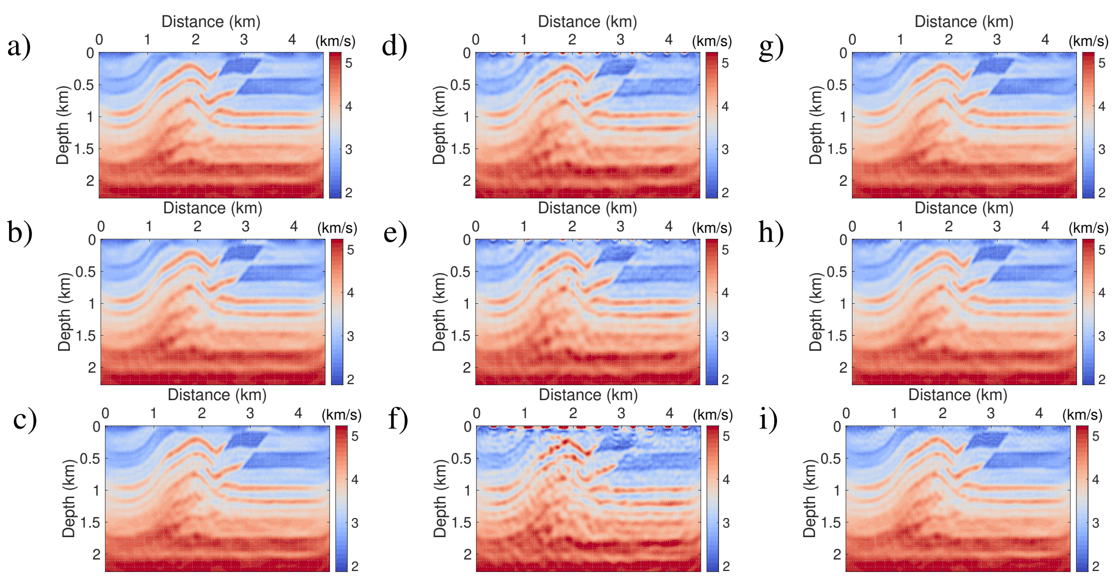

FIG. 15. The first column is the final inverted results of the KSW method using observed data with wavelet 1 (a), wavelet 2 (b), and wavelet 3 (c), respectively. The second column is the final inverted results of the old method using observed data with wavelet 1 (d), wavelet 2 (e), and wavelet 3 (f), respectively. The third column is the final inverted results of the old method using observed data with wavelet 1 (g), wavelet 2 (h), and wavelet 3 (i), respectively.

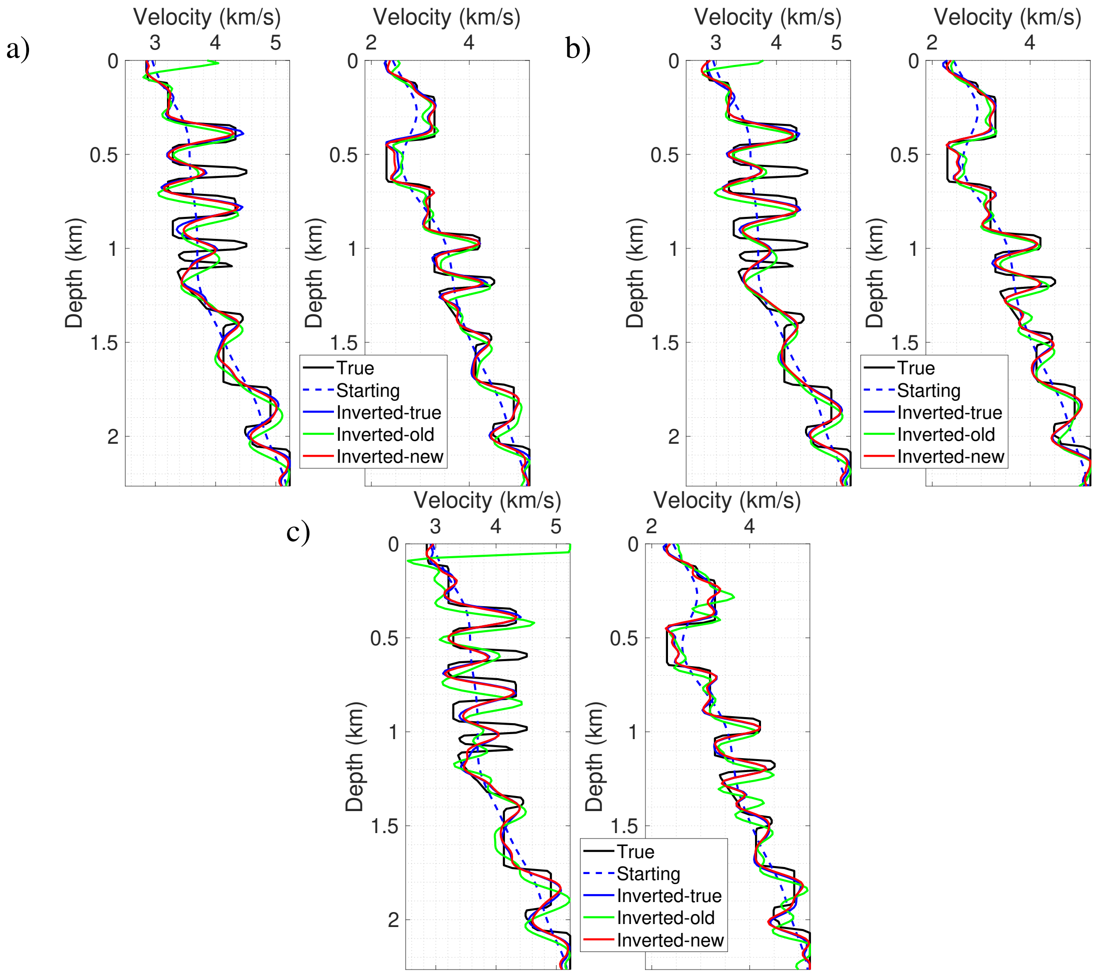

FIG. 16. Traces extracted at distances 1.5km and 2.5km from the results shown in Figure 15. (a), (b), and (c) are inverted traces of different methods using data with wavelet 1, wavelet 2, and wavelet 3, respectively. In each panel, the solid black line is the true model, the dashed blue line is the starting model, the solid blue line is the result of the KSW method, the solid green line is the result of the old method, and the solid red line is the result of the new method.

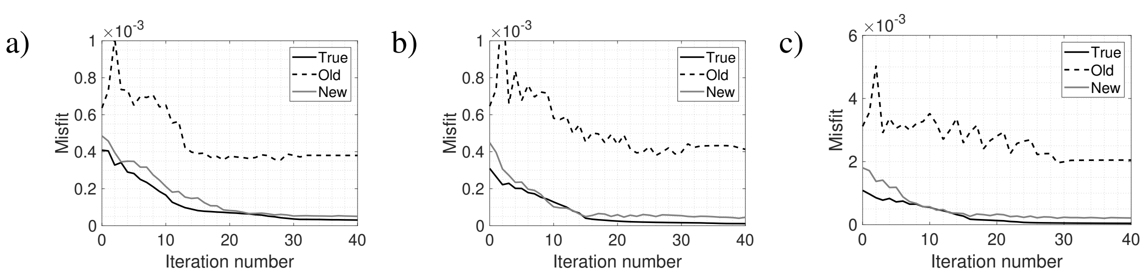

FIG. 17. Curves of the data misfit versus the iteration number for different methods using data with wavelet 1 (a), wavelet 2 (b), and wavelet 3 (c), respectively. In each panel, the black line is the data misfit curve for the KSW method, the dashed line is the data misfit curve of the old method, and the gray line is the data misfit curve of the new method.

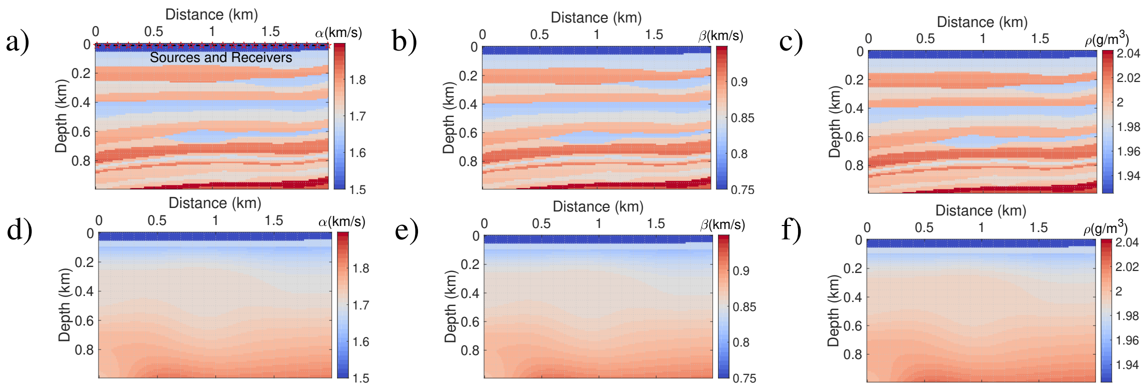

FIG. 18. (a) True P-wave velocity and acquisition geometries, (b) true S-wave velocity, (c) true density, (d) starting model of P-wave velocity, (e) starting model of S-wave velocity, (f) starting model of density. The dash lines and stars in (a) are the locations of receivers and sources, respectively.

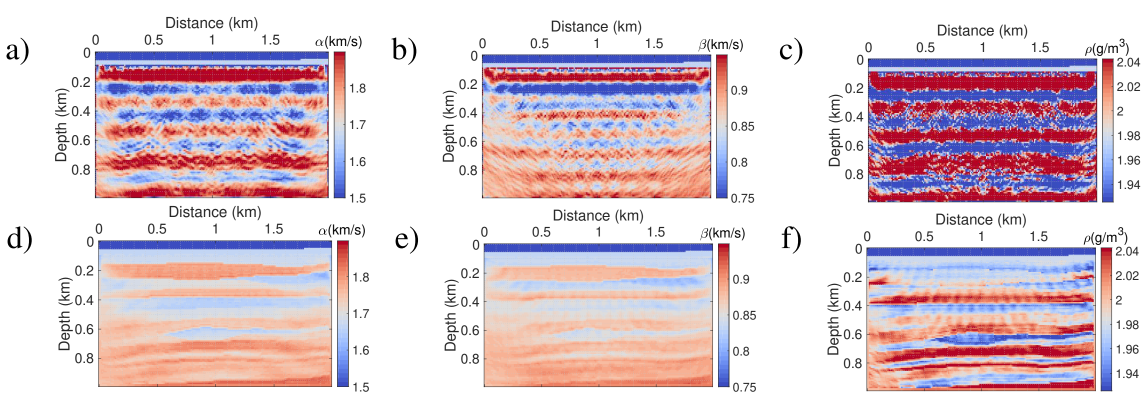

FIG. 19. Inverted results of the old method, (a) P-wave velocity, (b) S-wave velocity, (c) density, and inverted results of the new method, (d) P-wave velocity, (e) S-wave velocity, (f) density.

CONCLUSION

A robust source-independent FWI method has been developed in this paper, which has been demonstrated via tests of different starting models, different true models, different levels of random noise, and different source wavelets. It does not require any prior source wavelet information. It does not require an accurate starting model, even a 1D starting model is feasible to output an accurate wavelet estimate. It is stable for random noises. A good estimate of the source wavelet can be obtained from a poorly converged model based on the new proposed wavelet estimation equation. All in all, the performance of the new source-independent FWI in the tests is close to that of that of the KSW FWI.

ACKNOWLEDGEMENTS

We thank the sponsors of CREWES for continued support. This work was funded by CREWES industrial sponsors, NSERC (Natural Science and Engineering Research Council of Canada) through the grants CRDPJ 543578-19.

REFERENCES

Bunks, C., Saleck, F. M., Zaleski, S., and Chavent, G., 1995, Multiscale seismic waveform inversion: Geophysics, **60**, No. 5, 1457–1473.

Cheong, S., Shin, C., Pyun, S., Min, D.-J., and Suh, S., 2004, Efficient calculation of steepest descent direction for source-independent waveform inversion using normalized wavefield by convolution, *in* SEG Technical Program Expanded Abstracts 2004, Society of Exploration Geophysicists, 1842–1845.

Choi, Y., and Alkhalifah, T., 2011, Source-independent time-domain waveform inversion using convolved wavefields: Application to the encoded multisource waveform inversion: Geophysics, **76**, No. 5, R125–R134.

Choi, Y., and Min, D.-J., 2012, Source-independent elastic waveform inversion using a logarithmic wavefield: Journal of Applied Geophysics, **76**, 13–22.

Choi, Y., Shin, C., Min, D.-J., and Ha, T., 2005, Efficient calculation of the steepest descent direction for source-independent seismic waveform inversion: An amplitude approach: Journal of Computational Physics, **208**, No. 2, 455–468.

Fichtner, A., 2010, Full seismic waveform modelling and inversion: Springer Science & Business Media.

Fu, X., and Innanen, K. A., 2022, Time-lapse seismic imaging using shot gathers with non-repeatable source wavelets: Geophysics, **88**, No. 1, 1–108.

Fu, X., Keating, S., Innanen, K. A., and Hu, Q., 2020, Double-wavelet double-difference elastic full-waveform inversion: CREWES Report.

Lailly, P., Bednar, J. et al., 1983, The seismic inverse problem as a sequence of before stack migrations: Conference on Inverse Scattering, Theory and Application, Society for Industrial and Applied Mathematics, Expanded Abstracts, 206–220.

Lee, K. H., and Kim, H. J., 2003, Source-independent full-waveform inversion of seismic data: Geophysics, **68**, No. 6, 2010–2015.

Mora, P., 1987, Nonlinear two-dimensional elastic inversion of multioffset seismic data: Geophysics, **52**, No. 9, 1211–1228.

Pratt, R. G., 1999, Seismic waveform inversion in the frequency domain, part 1: Theory and verification in a physical scale model: Geophysics, **64**, No. 3, 888–901.

Pratt, R. G., Shin, C., and Hick, G., 1998, Gauss–newton and full newton methods in frequency–space seismic waveform inversion: Geophysical journal international, **133**, No. 2, 341–362.

Shin, C., Jang, S., and Min, D.-J., 2001, Improved amplitude preservation for prestack depth migration by inverse scattering theory: Geophysical prospecting, **49**, No. 5, 592–606.

Sirgue, L., and Pratt, R. G., 2004, Efficient waveform inversion and imaging: A strategy for selecting temporal frequencies: Geophysics, **69**, No. 1, 231–248.

Song, Z.-M., Williamson, P. R., and Pratt, R. G., 1995, Frequency-domain acoustic-wave modeling and inversion of crosshole data: Part ii—inversion method, synthetic experiments and real-data results: Geophysics, **60**, No. 3, 796–809.

Tarantola, A., 1984, Inversion of seismic reflection data in the acoustic approximation: Geophysics, **49**, No. 8, 1259–1266.

Virieux, J., and Operto, S., 2009, An overview of full-waveform inversion in exploration geophysics: Geophysics, **74**, No. 6, WCC1–WCC26.

Warner, M., and Guasch, L., 2016, Adaptive waveform inversion: Theory: Geophysics, **81**, No. 6, R429–R445.

Wu, R.-S., Luo, J., and Wu, B., 2014, Seismic envelope inversion and modulation signal model: Geophysics, **79**, No. 3, WA13–WA24.

Xu, K., Greenhalgh, S. A., and Wang, M., 2006, Comparison of source-independent methods of elastic waveform inversion: Geophysics, **71**, No. 6, R91–R100.

Zhang, Q., Zhou, H., Li, Q., Chen, H., and Wang, J., 2016, Robust source-independent elastic full-waveform inversion in the time domainrobust source-independent elastic fwi: Geophysics, **81**, No. 2, R29–R44.

Zhou, B., and Greenhalgh, S. A., 2003, Crosshole seismic inversion with normalized full-waveform amplitude data: Geophysics, **68**, No. 4, 1320–1330.